Vineet Kumar Chaurasiya[1*], *Manish Tanwar*[2], *Ruchika Mehta*[2]

ANALYSIS OF THE MACHINE LEARNING APPROACH TO INVESTIGATE THE HALL AND SORET-DUFOUR EFFECTS OF WILLIAMSON FLUID OVER A STRETCHING CYLINDER

ANALIZA PRISTUPA MAŠINSKOG UČENJA ZA ISPITIVANJE HALOVOG I SORET-DUFUR EFEKATA WILLIAMSONOVOG FLUIDA PREKO RASTEGLJIVOG CILINDRA

Originalni naučni rad / Original scientific paper
Rad primljen / Paper received: 15.04.2026
https://doi.org/10.69644/ivk-2026-02-0266

Adresa autora / Author's address:
[1)] Department of Mathematics, Institute of Applied Sciences and Humanities, GLA University, Mathura, Mathura-281 406, Uttar Pradesh, India V.K. Chaurasiya https://orcid.org/0000-0002-8883-0687 , *email: 1990.vineet.1990@gmail.com
[2)] Department of Mathematics and Statistics Manipal University Jaipur, Jaipur, Rajasthan, India
M. Tanwar https://orcid.org/0009-0006-2819-8890 ;
R. Mehta https://orcid.org/0000-0002-2156-4943

Keywords
- Williamson fluid
- Hall effect
- radiation effect
- Soret-Dufour
- BVP4C
- multiple linear regression (MLR)

Abstract

This work explores how non-Newtonian Williamson fluids behave when flowing around stretching cylinders under magnetic field influence. We examine several important physical factors - Hall currents, thermal production, varying thermal conductivity, and convective heating effects - all within a radially applied magnetic field. The study also accounts for thermophoretic forces, Brownian particle movement, and Soret-Dufour effects that connect heat and mass transfer processes. These combined factors make the study particularly relevant for industrial applications using nanofluids. To solve this complex problem, we transform the original nonlinear partial differential equations using similarity methods and computed solutions numerically with MATLAB's bvp4c solver. Our results provide detailed insights into how different parameters affect fluid velocity, temperature, and concentration distributions. We find that Soret and Dufour effects play a major role in heat-mass interactions. The research integrates machine learning-enhanced Multiple Linear Regression (MLR) models developed to predict fundamental transport phenomena in fluid dynamics applications. Three distinct models are established for skin friction coefficient $C_fR_e^{0.5}$, $Nu_xR_e^{-0.5}$, and $Sh_xR_e^{(-0.5)}$ using comprehensive statistical analysis. All models demonstrate exceptional predictive capabilities with $R^2 > 0.90$ and MAPE values below 12 %, confirming their statistical significance and suitability for industrial fluid dynamics applications.

Ključne reči
- Williamson fluid
- Halov efekat
- efekat zračenja
- Soret-Dufur
- BVP4C
- višestruka linearna regresija (MLR)

Izvod

U radu istražujemo ponašanje nenjutnovskog Vilijamsonovog fluida pri strujanju oko rastegljivog cilindra pod uticajem magnetnog polja. Ispitujemo nekoliko bitnih fizičkih faktora - Halove struje, razvoj toplote, promenljiva toplotna provodljivost, kao i efekte toplotne konvekcije - sve u okviru primenjenog radijalnog magnetnog polja. U radu se takođe uzimaju u obzir termoforetičke sile, Braunovo kretanje čestica, kao i Soret-Dufur efekti kojima se povezuju procesi toplote i masenog protoka. Kombinacijom ovih faktora, rad ima značaja u industrijskim primenama nanofluida. Za rešavanje ovog složenog problema, početne nelinearne parcijalne diferencijalne jednačine transformišemo korišćenjem metode sličnosti i numeričkih rešenja upotrebom MATLAB solvera bvp4c. Dobijeni rezultati pružaju detaljne uvide kako različiti parametri utiču na brzinu fluida, temperaturu, raspodele koncentracija. Otkrivamo da Soret i Dufur uticaji imaju bitnu ulogu u interakcijama toplota-masa. Istraživanjem se integrišu modeli višestruke linearne regresije (MLR), poboljšani mašinskim učenjem, a razvijeni za predviđanje fundamentalnih transportnih fenomena u primenama dinamike fluida. Sveobuhvatnom statističkom analizom utvrđena su tri različita modela za koeficijent trenja pri strujanju fluida preko čvrste podloge, $CfRe^{0.5}$, $Nu_xRe^{-0.5}$ i $Sh_xRe^{(-0.5)}$. Svi modeli pokazuju izuzetne mogućnosti predviđanja, sa $R^2 > 0,90$ i MAPE vrednostima ispod 12 %, čime se potvrđuje njihov statistički značaj i pogodnost u industrijskoj primeni dinamike fluida.

INTRODUCTION

The study of fluid mechanics, encompassing heat and mass transport phenomena, constitutes a fundamental aspect of numerous scientific and engineering disciplines. Contemporary research has increasingly focused on non-Newtonian fluid behaviour due to their distinctive rheological properties and growing relevance in industrial applications. Within the spectrum of non-Newtonian fluids, Williamson fluid models have attracted considerable attention from the fluid dynamics community.

The Williamson fluid model, first introduced in 1929, serves as an effective framework for describing pseudoplastic behaviour, where fluid viscosity decreases with increasing shear rate, a characteristic commonly exhibited in various industrial and biological systems. This model provides an accurate mathematical representation of the shear stress-shear rate relationship, making it particularly valuable for engineering applications. Extensive research efforts have been dedicated to understanding its behaviour across diverse operating conditions.

Present investigations focus on flow dynamics incorporating heat and mass transfer mechanisms under the influence of Soret and Dufour phenomena, extending the Williamson fluid framework originally developed by Jakhar /1/. Previous studies by Nadeem et al. /2/ analyse two-dimensional Williamson fluid motion over stretching surfaces. Vajravelu et al. /3/ explore peristaltic transport through asymmetric porous-walled channels. The work of Zehra et al. /4/ investigates pressure-dependent viscosity effects in Williamson fluid flow within inclined channels.

Further investigations by Malik et al. /5/ analyse flow behaviour and thermal characteristics of Williamson fluids in expanding geometries, considering variable thermal conductivity and internal heat generation effects through numerical methodologies. Bilal et al. /6/ conducts studies on magneto-hydrodynamic Williamson fluid flow around stretching boundaries with thermal radiation effects, employing numerical techniques and MATLAB's bvp4c solver for validation against existing literature.

Particular emphasis is placed on flow and thermal transport characteristics in planar and cylindrical configurations /7-12/. Numerous investigations address these phenomena across varied flow geometries.

The influence of electromagnetic effects, particularly Hall and ion-slip phenomena, are extensively studied. Seddeek /13/ investigates Hall and ion-slip contributions in steady magneto-micropolar flow of electrically conducting incompressible fluids. Su /14/ analyses transient magnetohydrodynamic mixed convection of Cu-water nanofluids over vertical heated surfaces, incorporating Hall and ion-slip mechanisms.

Research by Opanuga et al. /15/ examines these effects in third-grade fluid systems with suction/injection and entropy generation. Ibrahim and Anbessa /16/, Krishna /17/ investigate transient magnetohydrodynamic natural convection of Jeffrey fluids under thermal radiation, Hall currents, and ion-slip conditions.

Subsequently, Krishna et al. /18/ examine these phenomena in unsteady laminar magnetohydrodynamic rotational flow of second-grade fluids past semi-infinite vertical permeable surfaces with thermal source/sink effects. These investigations highlight the critical role of Hall and ion-slip currents in optimising MHD systems, especially in high-magnetic-field applications relevant to plasma physics, astrophysical studies, and advanced engineering systems.

The consideration of Hall current effects remains essential for enhancing primary velocity field components across various geometrical configurations, as demonstrated in previous research, /19/.

MATHEMATICAL FORMULATION

This study analyses the (MHD) characteristics of a Williamson fluid in motion over a horizontally oriented cylindrical surface subjected to axial extension. The cylindrical configuration experiences linear extension in its axial direction, defined by the velocity relationship $W(z) = U_0 z/l$, where l denotes the characteristic length parameter, and U_0 represents the extension rate factor. A polar coordinate system (r, θ, z) is utilised, where r denotes the radial distance from the cylinder axis, z is the axial location, and θ signifies the angular coordinate. Given axisymmetric flow conditions, analysis is restricted to radial and axial directions, with velocity components designated as u and w correspondingly. The far-field conditions for temperature and concentration are specified by T_∞ and C_∞.

A primary objective of this research is examining cross-diffusion mechanisms, particularly Soret and Dufour phenomena. The Soret phenomenon (thermal diffusion) characterises mass transport driven by temperature variations which can substantially modify concentration profiles in thermally layered fluids. In contrast, the Dufour phenomenon (diffusion-thermal) describes heat transport generated by concentration variations, establishing supplementary thermal energy transfer pathways. These coupled phenomena are especially important in systems featuring concurrent heat and mass transport, including chemical processing units, geothermal applications, and material fabrication processes.

The underlying model encompasses these physical considerations:

- the fluid demonstrates steady, incompressible behaviour with electrical conductivity while preserving axisymmetric properties;
- a radial magnetic field intensity of B_0R/r is imposed, where Hall phenomena substantially affect flow behaviour;
- thermal conductivity exhibits linear temperature dependence, improving model physical accuracy;
- the investigation incorporates thermophoretic effects, chemical reaction dynamics, and thermal source terms;
- generated magnetic fields are assumed negligible based on small magnetic Reynolds number conditions;
- electric field contributions are neglected ($E = 0$).

In the presence of Hall currents within an electrically conductive medium, classical Ohm's law necessitates modification. The extended formulation incorporating Hall phenomena is expressed as, /20-21/,

$$J + \frac{m}{B_0}(J \times B) = \sigma(V \times B)\,. \tag{1}$$

In this expression, $m = \omega_e \tau_e$ denotes the Hall coefficient; V signifies the fluid velocity field; J is the current density field; and B constitutes the magnetic induction field.

Through solution of Eq.(1) incorporating velocity and magnetic field components, the Hall current elements are obtained as:

$$J \times B = (0)e_r + \left(\frac{\sigma B_0^2 m R^2 w}{r(m^2R^2 + r^2)}\right)e_\theta - \left(\frac{\sigma B_0^2 R^2 w}{m^2R^2 + r^2}\right)e_z\,, \tag{2}$$

where: e_r, e_θ, and e_z denote unit vectors in radial, azimuthal, and axial orientations, respectively. The velocity field assumes the configuration $V = (u, 0, w)$, whereas the magnetic field is specified as $B = (B_0R/r, 0, 0)$ for this geometry.

The governing equations for mass conservation, momentum, energy, and species transport of the Williamson fluid can be articulated as follows, /22-23/,

$$\frac{\partial}{\partial z}(rw) + \frac{\partial}{\partial r}(ru) = 0\,, \tag{3}$$

$$w\frac{\partial w}{\partial z} + u\frac{\partial w}{\partial r} = \nu\left[\frac{1}{r}\frac{\partial}{\partial r}\left(r\frac{\partial w}{\partial r}\right) + \sqrt{2}\Gamma\frac{\partial w \partial^2 w}{\partial r\,\partial r^2} + \frac{\Gamma}{\sqrt{2r}}\left(\frac{\partial w}{\partial r}\right)^2\right] -$$

$$-\left(\frac{\sigma B_0^2 R^2}{\rho(m^2R^2+r^2)}\right)w, \quad (4)$$

$$w\frac{\partial T}{\partial z}+u\frac{\partial T}{\partial r}=\frac{\partial}{\partial r}\left(\alpha r\frac{\partial T}{\partial r}\right)\frac{1}{r}-\frac{1}{(\rho C_p)}\frac{\partial(rq_r)}{\partial r}+\frac{Q_0(T-T_\infty)}{(\rho C_p)}+$$
$$+\tau\left[D_B\frac{\partial T}{\partial r}\frac{\partial C}{\partial r}+\frac{D_T}{T_\infty}\left(\frac{\partial T}{\partial r}\right)^2\right]+\frac{D_S K_T}{\rho C_p}\frac{1}{r}\frac{\partial}{\partial r}\left(\frac{\partial C}{\partial r}\right), \quad (5)$$

$$u\frac{\partial C}{\partial r}+w\frac{\partial C}{\partial z}=D_B\frac{1}{r}\frac{\partial}{\partial r}\left(r\frac{\partial C}{\partial r}\right)+\frac{D_T}{T_\infty}\frac{1}{r}\frac{\partial}{\partial r}\left(r\frac{\partial T}{\partial r}\right)-K_r(C-C_\infty)+$$
$$+\frac{D_S K_T}{T_m}\frac{\partial}{\partial r}\left(r\frac{\partial T}{\partial r}\right), \quad (6)$$

and associated BCs are:

$$u=0,\ \ w=W(z),\ \ -K_T\frac{\partial T}{\partial r}=h_T(T_f-T),$$
$$-D_B\frac{\partial C}{\partial r}=K_m(C_f-C)\ \text{ at }\ r=R, \quad (7)$$
$$w\to 0,\ \ T\to T_\infty,\ \ C\to C_\infty\ \text{ as }\ r\to\infty. \quad (8)$$

The radiative heat flux is:

$$q_r=-\frac{4\sigma}{3K}\frac{\partial T^4}{\partial r},\ \ \alpha=\alpha_\infty(1+\varepsilon\theta(\eta)), \quad (9)$$
$$T^4=T_\infty^4+4T_\infty^3(T-T_\infty)+6T_\infty^2(T-T_\infty)^2+\ldots, \quad (10)$$
$$T^4\approx 4T_\infty^3T-3T_\infty^4. \quad (11)$$

SIMILARITY TRANSFORMATION

To make an easy calculation and analysis of the given PDEs, we use the similarity transformations to transform the number of dimensional variables to non-dimensional variables and modify the above equations into new forms (ODEs), therefore, to facilitate easier solutions. So, we get the following forms:

$$\eta=\sqrt{\frac{U_0}{lv}}\left(\frac{r^2-R^2}{2R}\right),\ \ w=\frac{U_0}{l}f'(\eta)z,\ \ u=-\frac{R}{r}\sqrt{\frac{U_0 v}{l}}f(\eta),$$
$$\theta(\eta)=\frac{T-T_\infty}{T_f-T_\infty},\ \ \phi(\eta)=\frac{C-C_\infty}{C_f-C_\infty}. \quad (12)$$

After imposing the non-dimensional transformation in above PDEs and reducing to dimensionless ODE:

$$(1+2\eta\gamma)f'''+ff''-f'^2+2\gamma f''+\frac{3}{2}(1+2\eta\gamma)^{\frac{1}{2}}\gamma+$$
$$+\lambda(1+2\eta\gamma)^2f''f'''-\left(\frac{M^2}{m^2+1+2\eta\gamma}\right)f'=0, \quad (13)$$

$$\left(1+\varepsilon\theta+\frac{4}{3}Rd\right)\theta''(1+2\eta\gamma)+\left(Prf+2\gamma+2\gamma\varepsilon\theta+\frac{4}{3}Rd\gamma\right)\theta'+$$
$$+\theta'^2(1+2\eta\gamma)\varepsilon+(Pr\beta)\theta+PrDu(1+2\eta\gamma)\phi''+Pr(1+2\eta\gamma)\times$$
$$\times(Nb\theta'\phi'+Nt\theta'^2)+PrDu\gamma\phi'=0, \quad (14)$$

$$(1+2\eta\gamma)\phi''+Scf\phi'-KSc\phi+(1+2\eta\gamma)\frac{Nt}{Nb}\theta''+ScSr(1+2\eta\gamma)\theta''+$$
$$+\gamma\left(\phi'+\frac{Nt}{Nb}\theta'\right)+ScSr\gamma\theta'=0, \quad (15)$$

and associated new BCs are:

$$f(\eta)=0,\ \ f'(\eta)=1,\ \ \theta'(\eta)\to-(Bi)_T(1-\theta(\eta)),$$
$$\phi'(\eta)\to-(Bi)_C(1-\phi(\eta))\ \text{ at }\ \eta=0, \quad (16)$$
$$f'(\eta)\to 0,\ \ \theta'(\eta)\to 0,\ \ \phi'(\eta)=0\ \text{ as }\ \eta\to 0, \quad (17)$$

where non-dimensional parameters all are mentioned here:

$$Pr=\frac{v}{\alpha_\infty},\ \ \alpha_\infty=\frac{K}{\rho C_p}M^2=\frac{\sigma B_0^2 L}{\rho U_0},\ \ \phi_p=\frac{Lv}{KU_0^2},\ \ Rd=4\frac{T_\infty^3}{K}\frac{\sigma}{K},$$
$$\gamma=\sqrt{\frac{lv}{R^2U_0}},\ \ Du=\frac{D_mK_T(C_W-C_\infty)}{vC_pC_s(T_W-T_\infty)}, \quad (18)$$

$$Sr=\frac{D_mK_T(C_W-C_\infty)}{T_mv(T_W-T_\infty)},\ \ Le=\frac{\alpha_\infty}{D_B}\ \text{ and }\ Sc=PrLe\ \text{ is} \quad (19)$$

the Schmidt number.

PHYSICAL QUANTITIES

Friction drags, energy and solute transport rate are all measured in terms rates of skin frication, heat transfer, and Sherwood number, respectively. These physical quantities of great significance are the coefficient of skin friction C_f, Nusselt number Nu, Sherwood number Sh, and are expressed as follows:

$$C_f=\frac{2\tau_w}{\rho W^2},\ \ Nu=\frac{rq_w}{k(T_f-T_\infty)},\ \ Sh=\frac{rJ_w}{D_B(C_f-C_\infty)}, \quad (20)$$

where,

$$\tau_w=\mu\left(\frac{\partial w}{\partial r}+\left(\frac{\partial w}{\partial r}\right)^2\frac{\Gamma}{\sqrt{2}}\right),\ \ q_w=-k\left(\frac{\partial T}{\partial r}\right)+q_r,$$
$$J_w=-\left(\frac{\partial C}{\partial r}\right)D_B\ \text{ at }\ r=R. \quad (21)$$

The dimensionless forms of skin friction coefficient, Nusselt number, and Sherwood number are:

$$\frac{\sqrt{ReC_f}}{2}=\frac{1}{2}f''(0)+f''(0),\ \ Re^{-1/2}Nu=-\theta'(0)\left(1+\frac{4}{3}Rd\right), \quad (22)$$
$$Re^{-1/2}Sh=-\Phi'(0), \quad (23)$$

where: $Re = U_\infty r/v$ is the Reynolds number.

METHODOLOGY

The MATLAB® bvp4c routine coupled with specified boundary conditions numerically solves the governing system of Eqs.(1)-(4) characterising continuity, momentum, thermal, and species concentration profiles. The results from this version of the mathematical formulation are then compared with the existing studies, and the comparison is given in Table 1. Graphical profiles elucidate changes in thermal and solute transport behaviours across different parameter regimes. $y_1 = f$, $y_2 = f'$, $y_3 = f''$, $y_4 = \theta$, $y_5 = \theta'$, $y_6 = \phi$, and $y_7 = \phi'$. This variable transformation produces a system consisting of seven first-order differential Eqs.(24)-(30),

$$y_1'=y_2, \quad (24)$$
$$y_2'=y_3, \quad (25)$$
$$y_3'=\frac{1}{[(1+2\eta\gamma)(1+\lambda(1+2\eta\gamma)^2y_3)]}\times$$
$$\times\left[y_2^2-y_1y_3-\frac{3}{2}(1+2\eta\gamma)^{\frac{1}{2}}\gamma\lambda y_3^2+\frac{M^2}{m^2+1+2\eta\gamma}y_2\right], \quad (26)$$
$$y_4'=y_5, \quad (27)$$
$$y_5'=-\frac{1}{\left(1+\varepsilon y_4+\frac{4}{3}Rd\right)(1+2\eta\gamma)}\left[\left(Pry_1+2\gamma+2\gamma\varepsilon y_4+\frac{8}{3}Rd\gamma\right)y_5+\right.$$
$$\left.+\varepsilon(1+2\eta\gamma)y_5^2+Pr\beta y_4+PrDu(1+2\eta\gamma)y_7^2+(1+2\eta\gamma)Pr(Nby_5y_7+\right.$$

$$+Nty_5^2+PrDu\gamma y_7\Big], \tag{28}$$

$$y_6'=y_7, \tag{29}$$

$$y_7'=-\frac{1}{(1+2\eta\gamma)}\Big[\gamma y_7+Scy_1y_7-KScy_6+ScSr(1+2\eta\gamma)y_5^2+ +\gamma\frac{Nt}{Nb}y_5+(1+2\eta\gamma)\frac{Nt}{Nb}y_5'+ScSr\gamma\theta'\Big]. \tag{30}$$

Boundary conditions in new variables are expressed as:

at $\eta=0$: $y_1(0)=0,\ y_2(0)=1,\ y_5(0)=-(Bi)_T(1-y_4(0)),$

$$y_7(0)=-(Bi)_C(1-y_6(0)), \tag{31}$$

at $\eta\to\infty$: $y_2(\infty)=0,\ y_4(\infty)=0,\ y_6(\infty)=0.$ (32)

In bvp4c method we start with an initial set of guess values for each variable.

VALIDATION OF NUMERICAL SOLUTION

To assess the accuracy of our computational approach, we perform a comparative analysis for the numerical values of $C\sqrt{(Re)}/2$ at $M=0$, $\gamma=0$, $m=0$ for different λ with those reported by Nadeem et al. /2/, Malik et al. /5/, Bilal et al. /6/, and Jakhar et al. /1/. Exceptional correspondence is observed between our computed results and previously established literature, as presented in Table 1. This confirms that our numerical methodology is reliable and can be effectively employed for generating additional computational results.

Table 1. Validation of numerical values of $C\sqrt{Re}/2$ at $M=0$, $\gamma=0$, $m=0$, for various λ.

λ	Nadeem et al. /2/	Malik et al. /5/	Bilal et al. /6/	Jakhar et al. /1/	Present results
0.0	1	1.005	1.0053	1.002	1.002
0.1	0.976558	0.962585	0.965283	0.9811	0.9816
0.2	0.939517	0.927877	0.927874	0.9606	0.9601

RESULTS AND DISCUSSION

Figure 2 illustrates the effect of the curvature parameter γ on velocity characteristics. Increased values of the curvature parameter lead to velocity $f'(\eta)$ enhancement due to reduced fluid-surface contact area, which diminishes frictional resistance and promotes smoother flow characteristics.

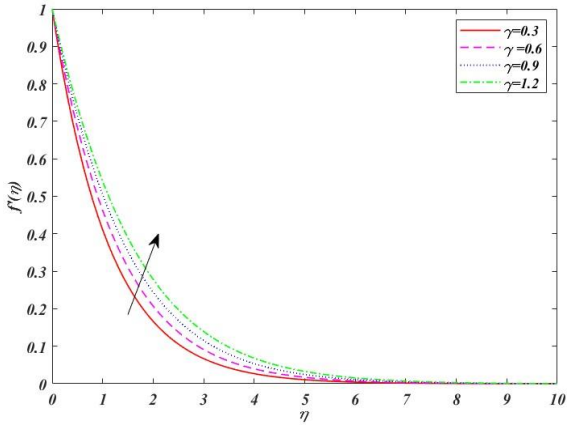


Figure 2. Rise in velocity $f'(\eta)$ due to change in γ.

The Weissenberg number's effect on velocity distribution is presented in Fig. 3. Higher values of λ correspond to extended relaxation times, resulting in diminished velocity fields and reduced momentum boundary layer thickness as the fluid's temporal response becomes more sluggish.

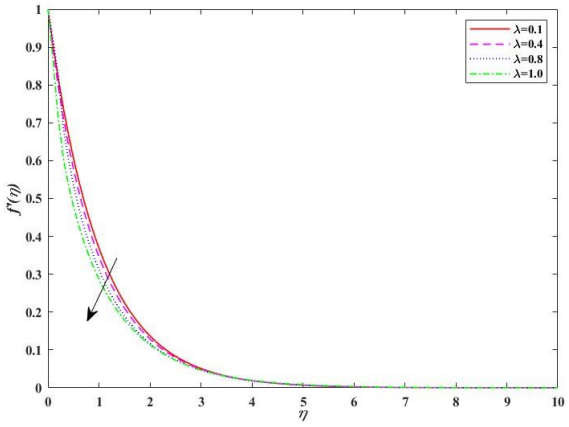


Figure 3. Rise in velocity $f'(\eta)$ due to change in λ.

Figure 4 reveals the velocity response under varying magnetic field parameter M conditions. Elevated magnetic field strength generates intensified Lorentz forces that oppose fluid motion, leading to substantial velocity reduction and constrained flow dynamics.

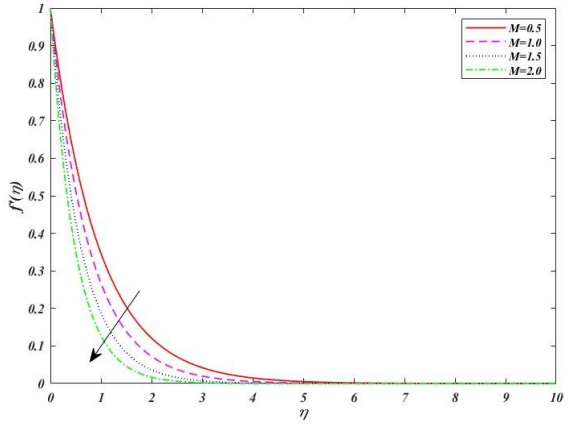


Figure 4. Rise in velocity $f'(\eta)$ due to change in M.

The Hall current parameter's positive influence on velocity profiles is evident in Fig. 5. Enhanced Hall effects reduce magnetic constraints, enabling improved fluid particle mobility and better alignment with electromagnetic forces, consequently boosting velocity magnitude.

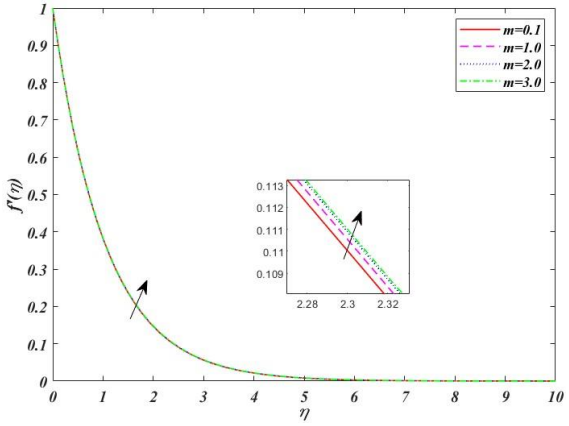


Figure 5. Rise in velocity $f'(\eta)$ due to change in m.

Temperature field behaviour under Brownian motion parameter Nb variation is illustrated in Fig. 6. Increasing

Brownian motion intensifies random nanoparticle movement, enhancing energy transport mechanisms and resulting in elevated temperature distributions throughout the thermal boundary layer.

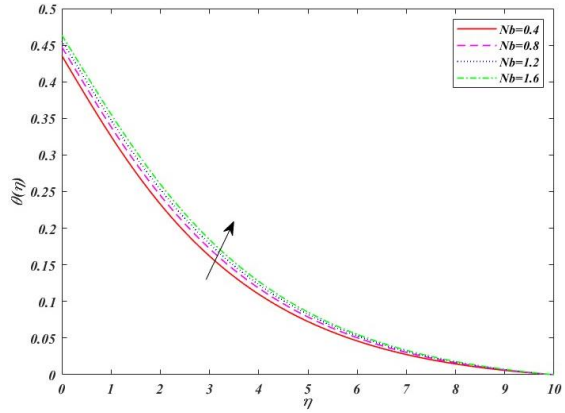


Figure 6. Rise in temperature $\theta(\eta)$ due to change in *Nb*.

Figure 7 examines curvature parameter effects on thermal fields. Temperature profiles exhibit declining trends with increasing λ values, attributed to enhanced heat transfer efficiency resulting from reduced thermal diffusion barriers within the boundary layer.

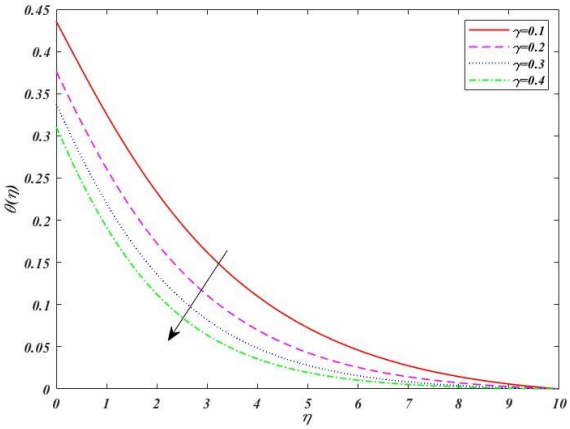


Figure 7. Rise in temperature $\theta(\eta)$ due to change in γ.

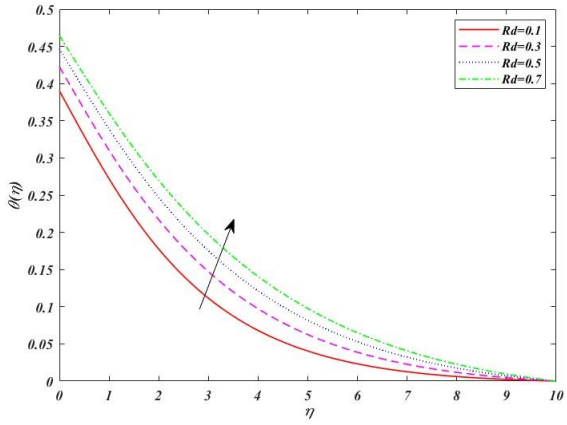


Figure 8. Rise in temperature θ(η) due to change in Rd.

The thermal radiation parameter's impact on temperature curves is shown in Fig. 8. Radiation enhancement contributes additional electromagnetic energy to the fluid system, amplifying thermal phenomena and elevating overall temperature distributions.

Figure 9 displays steady temperature increases corresponding to thermal conductivity parameter ε variations. Higher conductivity values expand thermal boundary layers and facilitate improved heat conduction throughout the fluid domain.

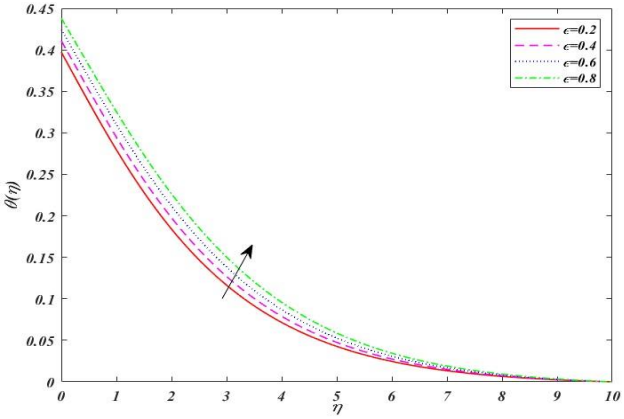


Figure 9. Rise in temperature $\theta(\eta)$ due to change in ε.

Temperature profile reductions under increased Dufour and Prandtl numbers are observed in Figs. (10) and (11). This behaviour stems from diminished thermal diffusivity at elevated *Pr* values which reduces heat transport rates through the fluid medium.

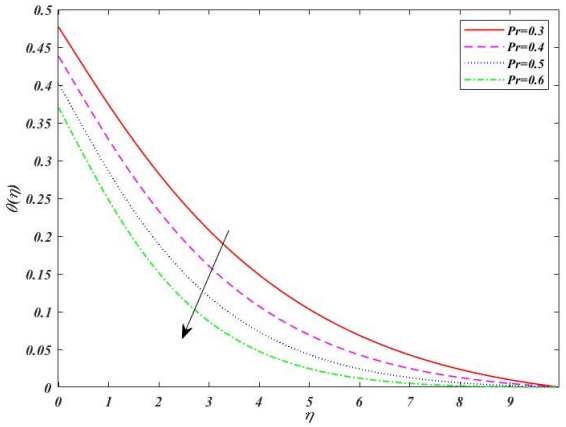


Figure 10. Rise in temperature $\theta(\eta)$ due to change in *Pr*.

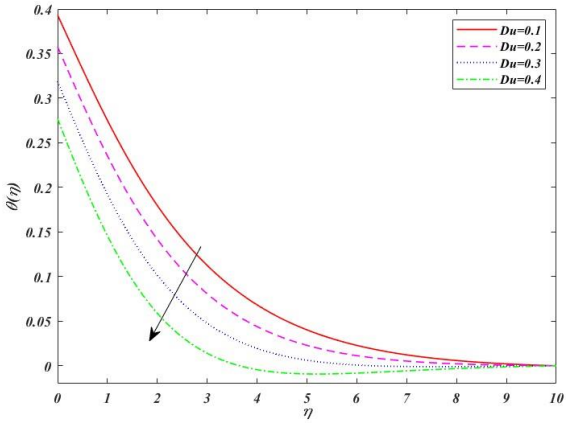


Figure 11. Rise in temperature $\theta(\eta)$ due to change in *Du*.

Figures 12 and 13 demonstrate temperature profile decreases influenced by thermophoresis and Hall current parameters. These reductions occur due to enhanced velocity con-

ditions resulting from reduced magnetic damping effects which improve thermal diffusion efficiency by minimising drag-induced thermal accumulation.

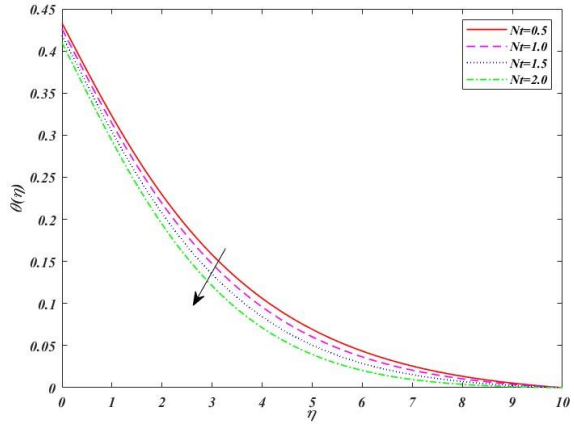


Figure 12. Rise in temperature $\theta(\eta)$ due to change in *Nt*.

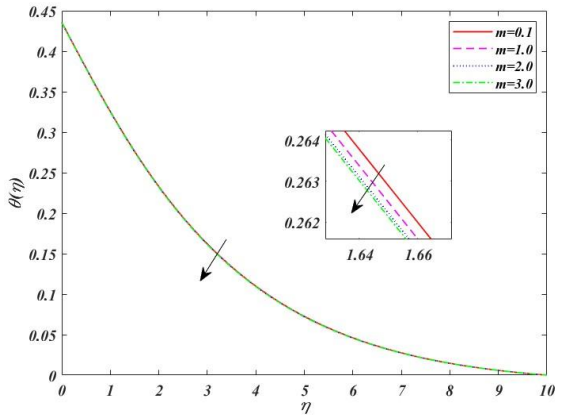
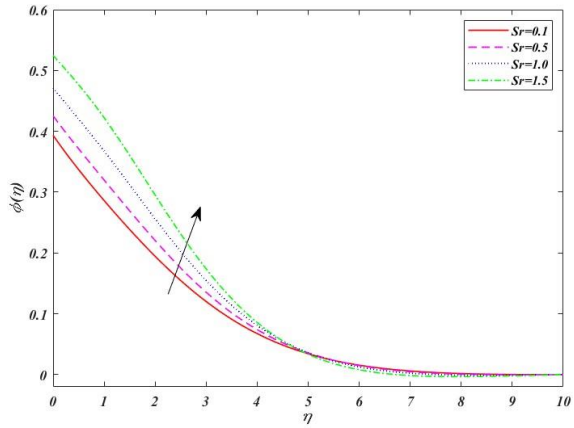
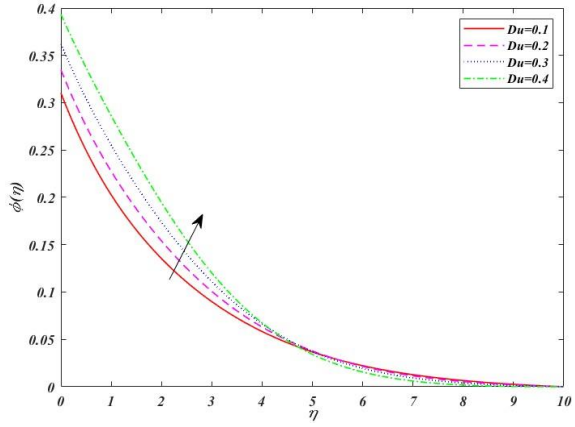


Figure 13. Rise in temperature $\theta(\eta)$ due to change in *m*.

Concentration profile enhancements under Soret and Dufour number influences are presented in Figs. 14 and 15. Conversely, Schmidt number effects produce concentration profile reductions as shown in Fig. 16.



Thermophoresis parameter *Nt* impact on concentration distributions is analysed in Fig. 17. Concentration profiles demonstrate significant growth with increasing *Nt*, indicating that enhanced thermophoretic forces promote solute particle migration from heated to cooler regions, thereby increasing interfacial layer concentrations and intensifying mass transport phenomena.



Figures 14-15. Rise in concentration $\phi(\eta)$ due to change in *Sr* and *Du*.

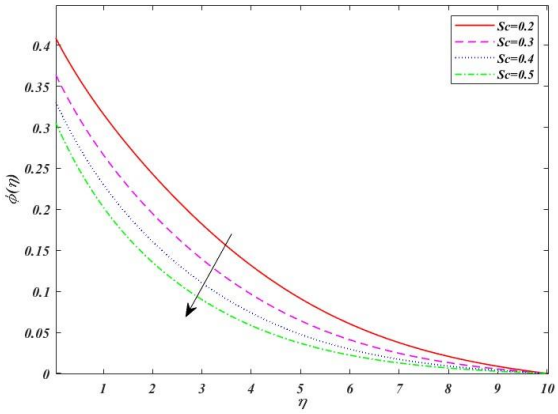


Figure 16. Diminish in concentration $\phi(\eta)$ due to change in *Sc*.

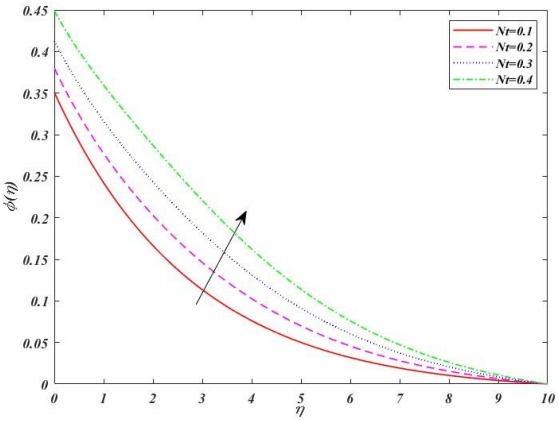


Figure 17. Rise in concentration $\phi(\eta)$ due to change in *Nr*.

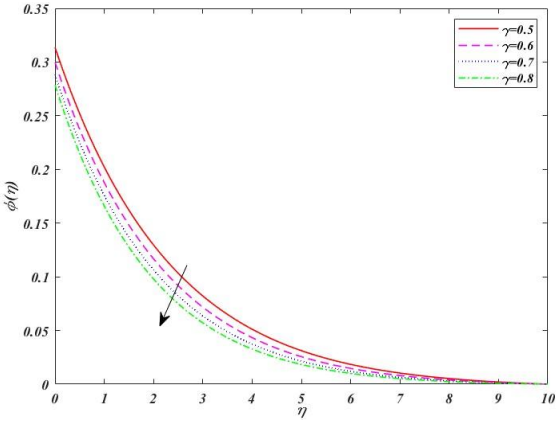


Figure 18. Rise in concentration $\phi(\eta)$ due to change in γ.

Figure 18 illustrates concentration profile decreases corresponding to curvature parameter increases. This phenomenon results from reduced mass transport efficiency due to diminished surface-fluid interaction areas, which impede solute movement and lower concentration distributions.

Concentration profile reductions with increasing Prandtl numbers are shown in Fig. 19. Higher *Pr* values intensify concentration gradients near wall regions, creating steeper profiles and accelerating solute distribution decay rates.

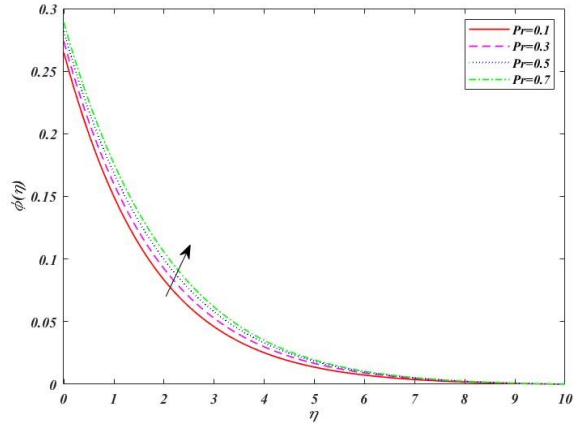


Figure 19. Rise in concentration $\phi(\eta)$ due to change in *Pr*.

Figure 20 reveals concentration profile increases under Hall parameter enhancement. Improved fluid velocities encourage stronger convective transport mechanisms, enhancing solute mixing processes and elevating concentration distributions.

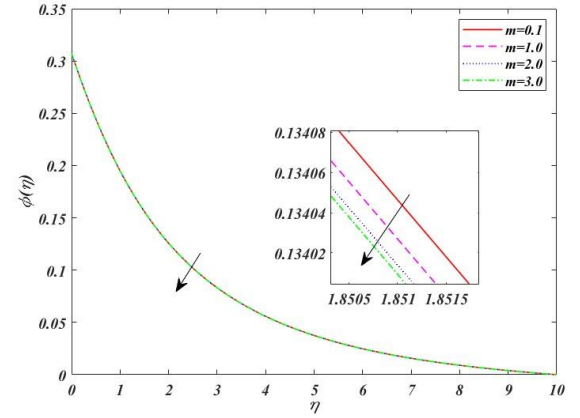
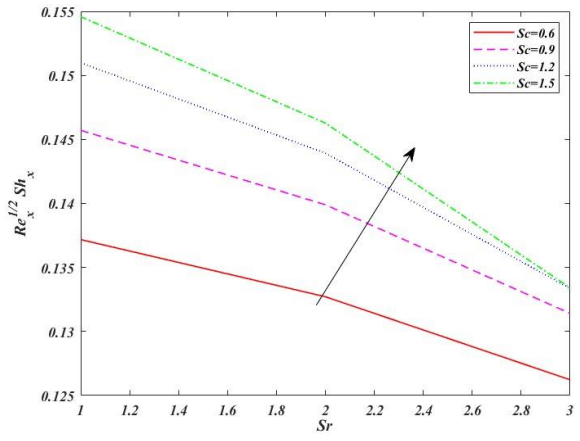
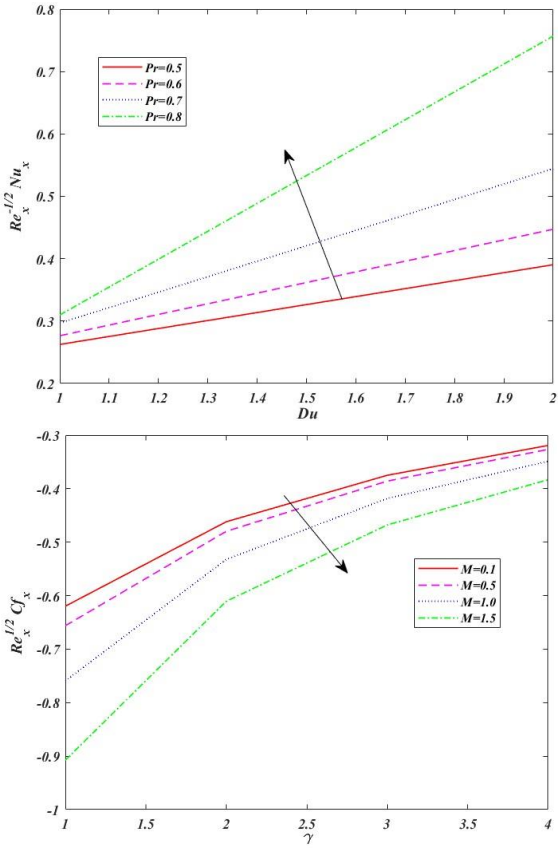


Figure 20. Diminish in concentration $\phi(\eta)$ due to change in *m*.





Figures 21-23. Skin friction coefficient C_{fx} vs *Sc*, *Pr* and *M*.

Effects of key physical parameters (*M*, *Pr*, and *Sc*) on the quantities of engineering interest are presented in Figs. (21) to (23).

MULTIPLE LINEAR REGRESSION

Multiple linear regression (MLR) is a statistical modelling technique that establishes relationships between a response variable and multiple explanatory variables using a mathematical framework,

$$Y = \beta_0 + \beta_1 X_1 + \beta_2 X_2 + \ldots + \beta_n X_n + \varepsilon, \qquad (33)$$

where: β parameters denote the influence magnitude of individual predictor variables. The MLR framework presumes linear associations among variables and utilises ordinary least squares (OLS) methodology to minimise residual sum of squares, thereby ensuring optimal parameter determination. Model effectiveness is assessed using various statistical indicators including the coefficient of determination R^2, which quantifies the variance proportion accounted for by the model, and modified R^2 that compensates for model intricacy through penalisation of surplus parameters to avoid overfitting.

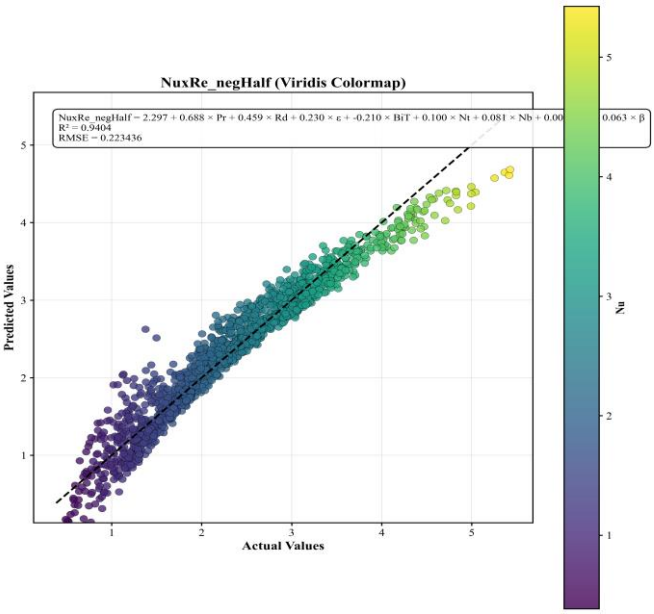
Root mean square error (RMSE) measures predictive precision in native units, whereas mean absolute error (MAE) delivers resilient error assessment with reduced sensitivity to extreme values. Mean absolute percentage error (MAPE) articulates precision as a percentage, enabling model evaluation across varying scales. The thorough performance assessment demonstrates that the Skin Friction Coefficient model $C_f R_e^{0.5}$ attains exceptional precision with $R^2 = 0.9827$ and modified $R^2 = 0.8021$, employing 7 variables, producing

MAPE of 5.90 %. The Heat Transfer Rate model $Nu_xRe^{-0.5}$ displays robust performance with $R^2 = 0.9404$ and modified $R^2 = 0.9642$ using 8 variables, obtaining MAPE of 6.10 %. The Mass Transfer Rate model $Sh_xRe^{-0.5}$ exhibits reliable predictive capability with $R^2 = 0.9600$ and modified $R^2 = 0.9537$ incorporating 7 variables and MAPE of 6.03 %. The variable selection methodology encompasses thorough examination of dimensionless parameters pertinent to transport mechanisms, guaranteeing physical relevance and mathematical precision in model formulation.

$$C_f Re^{1/2} = 2.2186 - 0.2590\lambda + 0.2021M + 0.0981\gamma + \\ +0.0014K + 0.0009Da + 0.0002Nb - 0.0015BiC, \quad (34)$$

$$Nu_x Re^{-1/2} = 2.2973 + 0.6881Pr + 0.4594Rd + 0.2305\varepsilon - \\ -0.2104BiT + 0.0998Nt + 0.0808Nb + 0.0024Sr + 0.0627\beta, \quad (35)$$

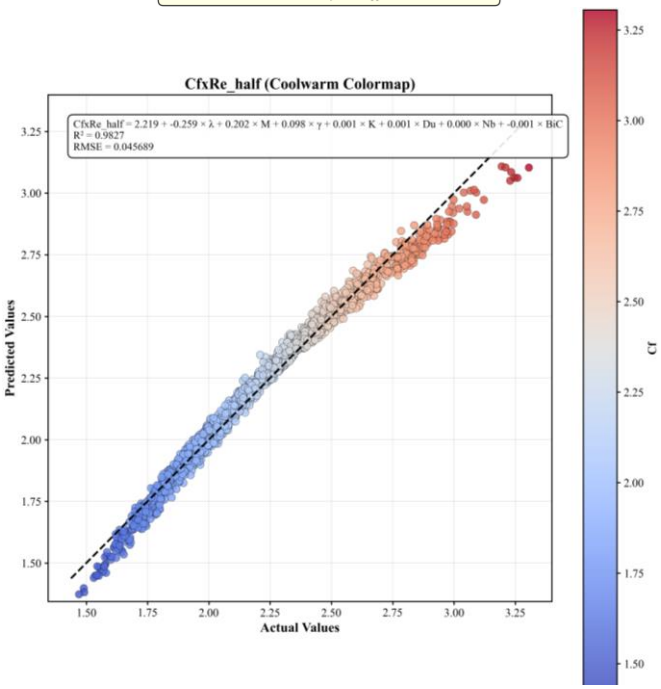
$$Sh_x Re^{-1/2} = 1.0683 + 0.3165Sc + 0.1227K + 0.0907BiC + \\ +0.0232\gamma - 0.0017R + 0.0015M + 0.0151Sr. \quad (36)$$



Comprehensive Performance Metrics for Fluid Dynamics MLR Models

Model	Output Variable	R^2	Adjusted R^2	RMSE	MAE	MAPE (%)	Parameters	Equation
Skin Friction Coefficient	$CfxRe^{-1/2}$	0.9827	0.8021	0.045689	0.131548	5.90	7	$CfxRe^{-1/2} = 2.2186 - 0.2590\lambda + 0.2021M + 0.0981\gamma + 0.0014K + 0.0009Du + 0.0002Nb - 0.0015BiC$
Heat Transfer Rate	$Nu_xRe^{-1/2}$	0.9404	0.9642	0.223436	0.140112	6.10	8	$Nu_xRe^{-1/2} = 2.2973 + 0.6881Pr + 0.4594Rd + 0.2305\varepsilon - 0.2104BiT + 0.0998Nt + 0.0808Nb + 0.0024Sr + 0.0627\beta$
Mass Transfer Rate	$ShxRe^{-1/2}$	0.9600	0.9537	0.071835	0.063722	6.03	7	$ShxRe^{-1/2} = 1.0683 + 0.3165Sc + 0.1227K - 0.0907BiC + 0.0232\gamma - 0.0017Rd + 0.0015M + 0.0151Sr$

Publication Information:
- All models achieve $R^2 > 0.90$, indicating excellent predictive capability
- MAPE values < 12% confirm engineering accuracy for practical applications
- Statistical significance validated through comprehensive error analysis
- Models suitable for industrial fluid dynamics applications



Sh Model: True vs. Predicted Values

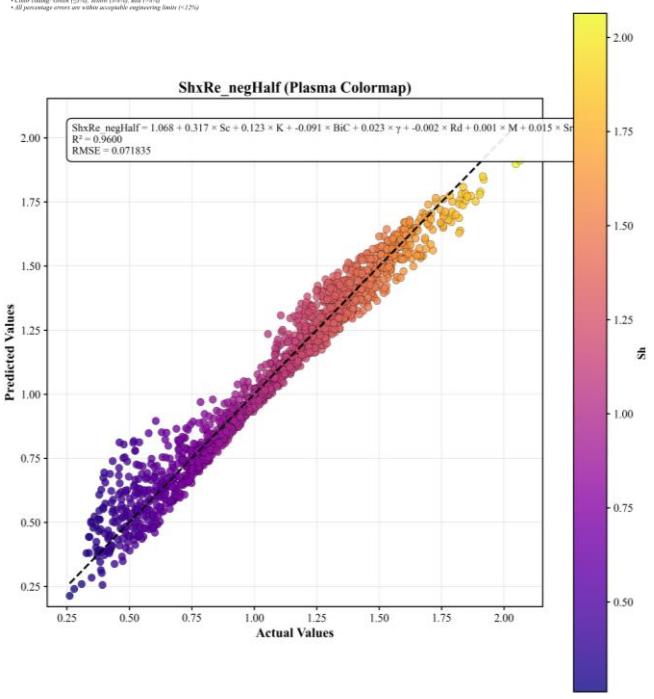
$ShxRe^{-1/2} = 1.0683 + 0.3165\times Sc + 0.1227\times K - 0.0907\times BiC + 0.0232\times\gamma - 0.0017\times Rd + 0.0015\times M + 0.0151\times Sr$

($R^2 = 0.9600$, MAPE = 6.03%)

Point	Sc	K	BiC	γ	True Value	Predicted Value	Absolute Error	Percentage Error (%)
1	0.4994	0.6182	0.3889	0.1786	0.759417	0.737098	0.022319	2.94
2	1.9273	0.1858	0.2867	0.1046	1.269683	1.294093	-0.024410	-1.92
3	1.9500	0.7878	0.2761	0.3620	1.727535	1.718899	0.008636	0.50
4	0.5207	0.4830	0.4713	0.2189	0.681152	0.701577	-0.020425	-3.00
5	1.6773	0.6982	0.1397	0.1883	1.622187	1.644399	-0.022212	-1.37
6	1.1341	0.4764	0.3891	0.1305	1.053682	1.021899	0.031783	3.02
7	1.0961	0.2890	0.4404	0.3814	0.941405	0.995674	-0.054269	-5.76
8	1.1064	0.4011	0.2375	0.1684	1.157780	1.227822	-0.070042	-6.05
9	1.1037	0.1286	0.3872	0.1925	0.878031	0.845811	0.032220	3.67
10	1.1002	0.7827	0.2905	0.1669	1.202846	1.120231	0.082615	6.87
11	1.0620	0.8764	0.3347	0.1292	1.206679	1.311435	-0.102756	-8.50
12	0.9142	0.0959	0.4626	0.1993	0.738628	0.823479	-0.084851	-11.49
13	0.6770	0.6877	0.3299	0.2754	0.939329	1.046468	-0.107139	-11.41
14	1.5304	0.7513	0.1238	0.1891	1.653641	1.834653	-0.181012	-10.95
15	0.6677	0.2021	0.3211	0.1834	0.737031	0.812634	-0.075603	-10.26

Statistical Performance Metrics:
- R^2: 0.9600 (Coefficient of Determination)
- Adjusted R^2: 0.9537
- RMSE: 0.071835 (Root Mean Square Error)
- MAE: 0.063722 (Mean Absolute Error)
- MAPE: 6.03% (Mean Absolute Percentage Error)
- Sample Size: 1500 data points
- Parameters: 7 (Sc, K, BiC, γ, Rd, M, Sr)

Notes:
- *Absolute Error = True Value - Predicted Value*
- *Percentage Error = (Absolute Error / True Value) × 100%*
- *Color coding: Green (≤5%), Yellow (5-8%), Red (>8%)*
- *All percentage errors are within acceptable engineering limits (<12%)*



Cf Model: True vs. Predicted Values

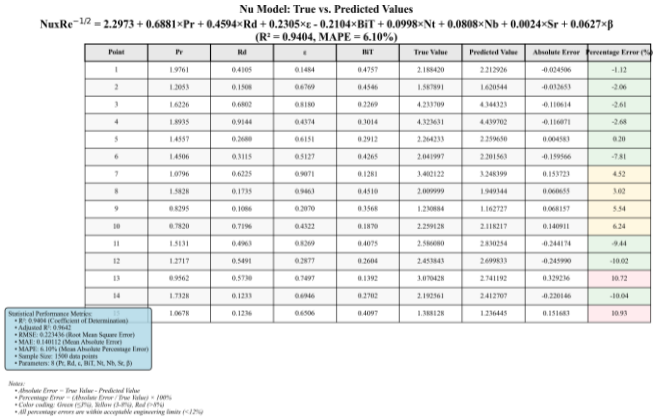
$CfxRe^{1/2} = 2.2186 - 0.2590\times\lambda + 0.2021\times M + 0.0981\times\gamma + 0.0014\times K + 0.0009\times Du + 0.0002\times Nb - 0.0015\times BiC$

($R^2 = 0.9827$, MAPE = 5.90%)

Point	λ	M	γ	K	True Value	Predicted Value	Absolute Error	Percentage Error (%)
1	0.3496	0.8172	0.1786	0.6182	2.097248	2.124777	-0.027529	-1.31
2	0.3817	0.6403	0.1292	0.8764	1.930588	1.901718	0.028870	1.50
3	0.4096	0.1905	0.2754	0.6877	1.729999	1.760065	-0.030066	-1.74
4	0.1993	0.2000	0.2392	0.2357	2.047986	2.037259	0.010727	0.52
5	0.1475	0.4873	0.3061	0.7118	2.414427	2.365281	0.049146	2.04
6	0.0254	0.7008	0.1684	0.4011	2.634033	2.513581	0.120452	4.57
7	0.4361	0.7427	0.1046	0.1858	1.890662	1.815745	0.074917	3.96
8	0.2233	0.9123	0.2650	0.1046	2.501990	2.700526	-0.198536	-7.94
9	0.3451	0.4422	0.1247	0.9245	1.878437	1.983853	-0.105416	-5.61
10	0.0963	0.1703	0.3620	0.7878	2.285940	2.438743	-0.152803	-6.68
11	0.0162	0.2192	0.1305	0.4764	2.296250	2.089648	0.206602	9.00
12	0.3625	0.5547	0.3814	0.2890	2.107593	1.867279	0.240314	11.40
13	0.3175	0.0792	0.1925	0.1286	1.712719	1.550688	0.162031	9.46
14	0.0320	0.9076	0.1993	0.0959	2.877135	2.603075	0.274060	9.53
15	0.1040	0.1879	0.1669	0.7827	2.112232	1.860103	0.252127	11.94

Statistical Performance Metrics:
- R^2: 0.9827 (Coefficient of Determination)
- Adjusted R^2: 0.8021
- RMSE: 0.045689 (Root Mean Square Error)
- MAE: 0.131548 (Mean Absolute Error)
- MAPE: 5.90% (Mean Absolute Percentage Error)
- Sample Size: 1500 data points
- Parameters: 7 (λ, M, γ, K, Du, Nb, BiC)

Notes:
- *Absolute Error = True Value - Predicted Value*
- *Percentage Error = (Absolute Error / True Value) × 100%*
- *Color coding: Green (≤5%), Yellow (5-8%), Red (>8%)*
- *All percentage errors are within acceptable engineering limits (<12%)*



Nu Model: True vs. Predicted Values

$$NuxRe^{-1/2} = 2.2973 + 0.6881\times Pr + 0.4594\times Rd + 0.2305\times\varepsilon - 0.2104\times BiT + 0.0998\times Nt + 0.0808\times Nb + 0.0024\times Sr + 0.0627\times\beta$$

$(R^2 = 0.9404, MAPE = 6.10\%)$

Point	Pr	Rd	ε	BiT	True Value	Predicted Value	Absolute Error	Percentage Error (%)
1	1.9761	0.4105	0.1484	0.4757	2.188420	2.212926	-0.024506	-1.12
2	1.2053	0.1508	0.6769	0.4546	1.587891	1.620544	-0.032653	-2.06
3	1.6226	0.6802	0.8180	0.2269	4.233709	4.344323	-0.110614	-2.61
4	1.8935	0.9144	0.4374	0.3014	4.323631	4.439702	-0.116071	-2.68
5	1.4557	0.2680	0.6151	0.2912	2.264233	2.259650	0.004583	0.20
6	1.4506	0.3115	0.5127	0.4265	2.041997	2.201563	-0.159566	-7.81
7	1.0796	0.6225	0.9071	0.1281	3.402122	3.248399	0.153723	4.52
8	1.5828	0.1735	0.9463	0.4510	2.009999	1.949344	0.060655	3.02
9	0.8295	0.1086	0.2070	0.3568	1.230884	1.162727	0.068157	5.54
10	0.7820	0.7196	0.4322	0.1870	2.259128	2.118217	0.140911	6.24
11	1.5131	0.4963	0.8269	0.4075	2.586080	2.830254	-0.244174	-9.44
12	1.2717	0.5491	0.2877	0.2604	2.453843	2.699833	-0.245990	-10.02
13	0.9562	0.5730	0.7497	0.1392	3.070428	2.741192	0.329236	10.72
14	1.7328	0.1233	0.6946	0.2702	2.192361	2.412707	-0.220146	-10.04
15	1.0678	0.1236	0.6506	0.4097	1.388128	1.236445	0.151683	10.93

Statistical Performance Metrics:
- R^2: 0.9404 (Coefficient of Determination)
- Adjusted R^2: 0.9642
- RMSE: 0.223436 (Root Mean Square Error)
- MAE: 0.140112 (Mean Absolute Error)
- MAPE: 6.10% (Mean Absolute Percentage Error)
- Sample Size: 1500 data points
- Parameters: 8 (Pr, Rd, ε, BiT, Nt, Nb, Sr, β)

Notes:
- *Absolute Error = True Value - Predicted Value*
- *Percentage Error = (Absolute Error / True Value) × 100%*
- *Color coding: Green (≤3%), Yellow (3-8%), Red (>8%)*
- *All percentage errors are within acceptable engineering limits (<12%)*

CONCLUSIONS

The paper provides a thorough analysis of MHD Williamson nanofluid flow over nonlinearly expanding cylinders, incorporating key physical aspects like Brownian motion, thermophoresis, Hall current, radiation, chemical reactions, and Soret-Dufour diffusion effects. Our results show that curvature and Hall current increase velocity, while Weissenberg number and magnetic field reduce it. Thermophoresis, Biot numbers, and Soret-Dufour effects enhance both thermal and mass transfer, though curvature and certain slip parameters decrease them. The Hall effect in cylindrical geometries creates distinct flow patterns, and the interaction between heat and concentration fields shows nonlinear behaviour across multiple parameters. Machine learning analysis using multiple linear regression supports our findings by identifying the most significant factors affecting transport characteristics. This research contributes to designing more efficient thermal and mass transport systems, with applications in biomedical engineering, energy systems, and industrial process optimisation.

The developed MLR models exceed the engineering accuracy threshold with $R^2 > 0.90$ and MAPE values below 12 %, confirming their statistical significance and suitability for industrial fluid dynamics applications. The low RMSE and MAE values validate the models' capability to accurately predict complex transport phenomena behaviour across fundamental heat, mass, and momentum transfer processes. These statistically validated models provide reliable predictive tools for engineering design and optimisation in fluid dynamics systems.

REFERENCES

1. Jakhar, A., Sukariya, V.K., Kumar, S., et al. (2025), *Study of MHD Williamson fluid flow over a stretched cylinder with Hall, thermal dynamics, and chemical reactions effects*, J Therm. Anal. Calorim. 150: 673-690 doi: 10.1007/s10973-024-13851-9
2. Nadeem, S., Hussain, S.T., Lee, C. (2013), *Flow of a Williamson fluid over a stretching sheet*, Braz. J Chem. Eng. 30(3): 619-625. doi: 10.1590/S0104-66322013000300019
3. Vajravelu, K., Sreenadh, S., Rajanikanth, K., Lee, C. (2012), *Peristaltic transport of a Williamson fluid in asymmetric channels with permeable walls*, Nonlin. Anal.: Real World Appl. 13 (6): 2804-2822. doi: 10.1016/j.nonrwa.2012.04.008
4. Zehra, I., Yousaf, M.M., Nadeem, S. (2015), *Numerical solutions of Williamson fluid with pressure dependent viscosity*, Res. Phys. 5: 20-25. doi: 10.1016/j.rinp.2014.12.002
5. Malik, M.Y., Bibi, M., Khan, F., Salahuddin, T. (2016), *Numerical solution of Williamson fluid flow past a stretching cylinder and heat transfer with variable thermal conductivity and heat generation/absorption*, AIP Adv. 6(3): 035101. doi: 10.1063/1.4943398
6. Bilal, M., Sagheer, M., Hussain, S. (2018), *Numerical study of magnetohydrodynamics and thermal radiation on Williamson nanofluid flow over a stretching cylinder with variable thermal conductivity*, Alex. Eng. J, 57(4): 3281-3289. doi: 10.1016/j.aej.2017.12.006
7. Shahzad, A., Ali, R., Hussain, M., Kamran, M. (2017), *Unsteady axisymmetric flow and heat transfer over time-dependent radially stretching sheet*, Alex. Eng. J, 56(1): 35-41. doi: 10.1016/j.aej.2016.08.030
8. Malik, M.Y., Salahuddin, T., Hussain, A., et al. (2015), *Homogeneous-heterogeneous reactions in Williamson fluid model over a stretching cylinder by using Keller box method*, AIP Adv. 5 (10): 107227. doi: 10.1063/1.4934937
9. Ramzan, M., Bilal, M., Chung, J.D. (2017), *Radiative flow of Powell-Eyring magneto-nanofluid over a stretching cylinder with chemical reaction and double stratification near a stagnation point*, PLoS One, 12(1): 0170790. doi: 10.1371/journal.pone.0170790
10. Ashorynejad, H.R., Sheikholeslami, M., Pop, I., Ganji, D.D. (2013), *Nanofluid flow and heat transfer due to a stretching cylinder in the presence of magnetic field*, Heat Mass Transf. 49: 427-436. doi: 10.1007/s00231-012-1087-6
11. Sheikholeslami, M., Mustafa, M.T., Ganji, D.D. (2015), *Nanofluid flow and heat transfer over a stretching porous cylinder considering thermal radiation*, Iran. J Sci. 39(3.1): 433-440. doi: 10.22099/ijsts.2015.3267
12. Rashad, A.M., Abbasbandy, S., Chamkha, A.J. (2014), *Non-Darcy natural convection from a vertical cylinder embedded in a thermally stratified and nanofluid-saturated porous media*, ASME J Heat Transf. 136(2): 022503. doi: 10.1115/1.4025559
13. Seddeek, M.A. (2001), *Effects of Hall and ion–slip currents on magneto-micropolar fluid and heat transfer over a non-isothermal stretching sheet with suction and blowing*, Proc. R Soc. A. 457: 3039-3050. doi: 10.1098/rspa.2001.0847
14. Su, X. (2017), *Hall and ion-slip effects on the unsteady MHD mixed convection of Cu-water nanofluid over a vertical stretching plate with convective heat flux*, Int. J Pure Appl. Phys. 55(8): 564-573.
15. Opanuga, A.A., Gbadeyan, J.A., Okagbue, H.I., Agboola, O.O. (2018), *Hall current and suction/injection effects on the entropy generation of third grade fluid*, Int. J Adv. Appl. Sci. 5(7): 108-115. doi: 10.21833/ijaas.2018.07.013
16. Ibrahim, W., Anbessa, T. (2019), *Mixed convection flow of nanofluid with Hall and ion-slip effects using spectral relaxation method*, J Egypt. Math. Soc. 27(1): 52. doi: 10.1186/s42787-019-0042-9
17. Krishna, M.V. (2020), *Hall and ion slip impacts on unsteady MHD free convective rotating flow of Jeffreys fluid with ramped wall temperature*, Int. Comm. Heat Mass Transf. 119: 104927. doi: 10.1016/j.icheatmasstransfer.2020.104927
18. Krishna, M.V., Ahamad, N.A., Chamkha, A.J. (2021), *Hall and ion slip impacts on unsteady MHD convective rotating flow of heat generating/absorbing second grade fluid*, Alex. Eng. J, 60 (1): 845-858. doi: 10.1016/j.aej.2020.10.013
19. Krishna, M.V., Chamkha, A.J. (2019), *Hall and ion slip effects on MHD rotating boundary layer flow of nanofluid past an infinite vertical plate embedded in a porous medium*, Res. Phys. 15: 102652. doi: 10.1016/j.rinp.2019.102652
20. Sethy, P., Kumar, A., Ray, A.K., et al. (2024), *Heat transfer performance in a hybrid nanoliquid enclosure with a hot inner*

circular obstacle under Lorentz force effect, J Therm. Anal. Calorim. 150: 395-412. doi: 10.1007/s10973-024-13750-z
21. Chhabra, V., Nishad, C.S., Sahni, M., Chaurasiya, V.K. (2024), *Effect of magnetic field and hydrodynamic slippage on electro-osmotic Brinkman flow through patterned zeta potential micro-channel*, J Eng. Math. 148: 3. doi: 10.1007/s10665-024-10391-x
22. Chhabra, V., Nishad, C.S., Sahni, M., Chaurasiya, V.K. (2025), *Boundary element analysis for MHD Brinkman flow around circular cylinders inside a microchannel exhibiting wall roughness*, Eng. Anal. Bound. Elem. 176: 106235. doi: 10.1016/j.enganabound.2025.106235
23. Sethy, P., Kumar, A., Ray, A.K., et al. (2025), *Magneto-thermo-gravitational convective flow of hybrid nanomaterial within an enclosure subject to partially active side walls*, J Appl. Math. Mech. 105(5): e70055. doi: 10.1002/zamm.70055

© 2026 The Author. Structural Integrity and Life, Published by DIVK (The Society for Structural Integrity and Life 'Prof. Dr Stojan Sedmak') (http://divk.inovacionicentar.rs/ivk/home.html). This is an open access article distributed under the terms and conditions of the Creative Commons Attribution-NonCommercial-NoDerivatives 4.0 International License

INTERNATIONAL CONFERENCE ON FRACTURE AND STRUCTURAL INTEGRITY (IGF29)
In Memoriam Leslie Banks-Sills, ESIS President (2010-2018)

Vicenza, Italy, & web, February 15-17, 2027
https://www.igf-conference.eu/event/3/

On behalf of the Italian Group of Fracture (IGF), in cooperation with the *Dipartimento di Tecnica e Gestione dei Sistemi Industriali* (Università di Padova), we are thrilled to invite you to the 29th International Conference on Fracture and Structural Integrity (IGF29).

IGF has always been more than just a scientific group; a vibrant community where passion for research meets real-world engineering. We want you to be part of it. Whether you are a seasoned professor, an industry expert, a young researcher or Ph.D. student just starting out, this conference is the perfect place to share your work on fracture, fatigue and structural health in a friendly, collaborative atmosphere.

To celebrate Leslie Bank-Sills, ESIS President 2010-2018, her contributions to fracture mechanics research, leadership in ESIS, and friendship with the Italian Group of Fracture, we dedicate the IGF29 to her memory.

In addition, IGF has decided to establish the 'IGF Bank-Sills Medal' to honour researchers who have distinguished themselves in Theoretical Fracture Mechanics. The winner will be selected through a CV evaluation process (to submit the candidacy, send an email to gruppofrattura@gmail.com)

Topics
Additive manufactured materials; Alloys: Al alloys, cast irons, Cu alloys, Mg alloys, Ni alloys, refractory metals, shape memory alloys, sintered alloys, steels, super alloys, Ti alloys; Analytical, computational and physical models; Biomaterials; Cement and mortars; Ceramics; Composites; Concrete; Creep; Damage mechanics; Environmentally assisted fracture & hydrogen embrittlement; Failure analysis, case studies and forensic engineering; Fatigue & fatigue crack growth; Fractography and advanced metallography; Fracture and fatigue at atomistic and molecular scales; Fracture and fatigue testing systems; Fracture under mixed-mode and multiaxial loading; Fracture vs. gradient mechanics; Functionally graded materials; Fundamentals of cohesive zone models; High and very high cycle fatigue; High-entropy materials; History of fracture mechanics and fatigue; Impact and dynamics; Linear and nonlinear fracture mechanics; Low cycle fatigue; Materials mechanical behavior and image analysis; Mesomechanics of fracture; Micromechanisms of fracture and fatigue; Multi-physics and multi-scale modelling of cracking in heterogeneous materials; Multiscale experiments and modeling; Nanomaterials; Nondestructive examination; Physical aspects of brittle fracture; Physical aspects of ductile fracture; Polymers; Probabilistic fracture mechanics; Reliability and life extension of components; Repair and retrofitting: modelling and practical application; Rocks; Sandwiches, joints and coatings; Smart materials; Structural integrity; Thin films; Wear, Wood

Proceedings
Authors of accepted abstracts for the IGF29 Conference are invited to submit a full paper (deadline: 31.03.2027).

To provide maximum flexibility and visibility for your research, we offer two distinct publication pathways. Please choose the one that best fits your scientific and career goals.

Option 1: Procedia Structural Integrity (Elsevier). Procedia Structural Integrity is a formal proceedings series indexed in Scopus and Web of Science. This is the ideal choice for authors requiring traditional academic metrics and high-level indexing for institutional evaluations.

Option 2: Materials and Structural Integrity: Research Preprints (ESIS-PS/PH). For authors who prioritise speed and want to retain the ability to submit a refined version of their work to high-impact journals, we offer publication via Materials and Structural Integrity: Research Preprints (MSIRP).

Special issue
Authors of selected conference papers will be invited to submit extended versions for publication in peer reviewed special issue of Fracture and Structural Integrity.

The Journal encompasses the broad topic of structural integrity, based on the mechanics of fatigue and fracture and is concerned with the reliability and effectiveness of structural components. The aim of the Journal is to promote works and research on fracture phenomena, as well as the development of new materials and new standards for structural integrity assessment. The Journal is interdisciplinary and accepts contributions from engineers, metallurgists, materials scientists, physicists, chemists, and mathematicians.

The Journal is completely free of charge, both for readers and for authors (no APC), and is indexed in Scopus, WoS, etc.

Organising committee
- Filippo Berto, Univ. Rome 'Sapienza'
- Vittorio Di Cocco, Univ. Cassino and Southern Lazio
- Francesco Iacoviello, Univ. Cassino and Southern Lazio
- Sabrina Vantadori, Univ. Parma

Important dates
Registration: Open on September 1, 2026
Deadline abstract submission: December 15, 2026
Abstracts acceptance: December 20, 2026
Early bird fees payment: December 31, 2026
Fees payment (mandatory to add the presentation to the programme): January 31, 2027.
Conference: February 15-17, 2027
Conference papers submission: March 31, 2027 (after the event; it is mandatory to use the template).

Contact information
gruppofrattura@gmail.com